



Vacancy engineering of group VI anions in NiCo₂A₄ (A = O, S, Se) for efficient hydrogen production by weakening the shackles of hydronium ion

Wei Zong^a, Ruqian Lian^b, Guanjie He^c, Hele Guo^a, Yue Ouyang^a, Jing Wang^d, Feili Lai^{a, **}, Yue-E. Miao^a, Dewei Rao^e, Dan Brett^c, Tianxi Liu^{a, *}

^a State Key Laboratory for Modification of Chemical Fibers and Polymer Materials, College of Materials Science and Engineering, Innovation Center for Textile Science and Technology, Donghua University, Shanghai, 201620, PR China

^b Key Laboratory of Physics and Technology for Advanced Batteries, Ministry of Education, College of Physics, Jilin University, Changchun, Jilin, 130012, PR China

^c Electrochemical Innovation Lab, Department of Chemical Engineering, University College London, London, WC1E 7JE, UK

^d School of Chemical Engineering and Energy, Zhengzhou University, Zhengzhou, 450001, PR China

^e School of Materials Science and Engineering, Jiangsu University, Zhenjiang, Jiangsu, 212013, PR China

ARTICLE INFO

Article history:

Received 30 June 2019

Received in revised form

27 November 2019

Accepted 13 December 2019

Available online 16 December 2019

Keywords:

Anionic vacancy

Group six element

Nickel cobalt selenide

Hydrogen evolution reaction

Hydronium ion

ABSTRACT

Hydrogen evolution reaction (HER) has been severely suppressed by the first proton adsorption step, due to the “shackles” of the surrounding water in the form of hydronium ions (H₁₃O₆⁺). Here, it has been found anionic vacancies in NiCo₂A₄ (A = O, S, Se) can weaken the shackles of surrounding water in H₁₃O₆⁺, resulting into efficient capture of H⁺ to form a H⁺-enriched field. Taking selenium vacancy-rich NiCo₂Se₄ nanowires on nitrogen-doped carbon nanofibers as an example, it displays higher electrocatalytic activities with low overpotential of 168 mV at 10 mA cm⁻² and a Tafel slope of 49.8 mV dec⁻¹. The HER performance is strongly related to the anionic vacancy size, the larger the anionic vacancy size is (V_{Se} > V_S > V_O), the higher the HER activity does. Guided by density functional theory calculations, it is found that the point defect structures can not only strengthen its interfacial linkage force with H⁺ by weakening the hydration force of contiguous hydronium ion, but also increase its charge density for efficient electron transfer to adsorbed H⁺. Therefore, this work creates a useful strategy to optimize the HER performance of traditional bimetallic compounds by engineering the solid-liquid-gas three-phase interfacial interaction.

© 2019 Published by Elsevier Ltd.

1. Introduction

Against the background of increasing consumption of fossil fuels, hydrogen has drawn great attention as a promising sustainable energy carrier due to its high gravimetric energy density, ability to be derived from renewable energy sources, and environmental friendliness (zero emissions at point of use) [1–10]. Among various technologies, the electrochemical hydrogen evolution reaction (HER) is regarded as one of the most promising methods for hydrogen production, making the development of high-efficiency electrocatalysts an area of intense research [11]. To

date, platinum and platinum-group-based metals are predominantly used as the electrocatalysts for the HER, with the challenge of high cost and low crustal abundance impeding commercial use and further scale-up. Therefore, it is imperative to discover and develop high-efficiency, low-cost, and alternative non-noble metal electrocatalysts (e.g. transition-metal carbides [12,13], oxides [14,15], sulfides [16,17], selenides [18–20]).

Generally, free H⁺ exhibits low adsorption energy during the HER process (Eqs. (1) and (2)) in acidic solution. However, it tends to form the hydronium ions (commonly formulated as H₁₃O₆⁺) by surrounding water molecules via strong hydrogen-bond interactions, where each H_(aq)⁺ ion in water solvent is surrounded by six water molecules to form a much more stable hydronium ion [21–24]. As a result, the positive charge density of H⁺ is dramatically decreased owing to the hydration effect, which hinders the efficient adsorption of H⁺ on the surface of electrocatalyst. From the

* Corresponding author.

** Corresponding author.

E-mail addresses: flilai14@fudan.edu.cn (F. Lai), txliu@dh.u.edu.cn (T. Liu).

perspective of physical chemistry, the adsorption of H^+ is regarded as the rate-determining step [25], making the hydration act as a bottleneck for the HER process. Recently, Feng et al. [26] discovered an efficient way to eliminate the effect of coordinate water molecules around H^+ by constructing polyaniline (PANI) nanodots-decorated CoP supported on carbon fibers, leading to an enhanced electrocatalytic activity toward HER. This ingenious multi-dimensional structure inspires us that surface engineering may be an ideal strategy to avoid the hydration effect in metal-based electrocatalysts by creating a 3-phase boundary of electrocatalyst, electrolyte, and H_2 gas during HER process. Recently, it has been reported that multi-transition metal-based compounds of group VI, nickel-cobalt-based oxide/sulfide/selenide [$NiCo_2A_4$ ($A = O, S, Se$)], display excellent electrocatalytic performance for the HER. According to our previous work, Lai et al. prepared a series of $NiCo_2O_4$ nanosheets wrapped hollow nitrogen-doped carbon polyhedrons with doped transition-metal domains, which are beneficial to boosting the electrocatalysis towards overall water splitting. The enhanced performance is attributed to the synergistic effects of energy level matching for electron transfer, and partial charge delocalization-induced rich active sites for reactant adsorption [27]. As demonstrated by Xue et al., this work reported GD-supported bifunctional electrodes using 3D GD foam as scaffolds and $NiCo_2S_4$ nanowires as building blocks, which exhibits outstanding catalytic activity and stability toward both OER and HER [28]. Furthermore, Fang et al. present a novel insight into tuning the HER electrocatalytic properties in Ni/Co-based HER electrocatalysts. The metallic nature and the synergistic effect of Ni/Co atoms favor the electron transfer kinetics between the catalyst and current collector, and the moderate electron delocalization reduces the barrier of proton binding, thus favoring the HER kinetics [29]. This is attributed to their high electrical conductivity [30,31], versatile redox nature [32,33] and hybrid orbitals [29,34], applying larger sizes of anions could expose more active sites with multivalent states for HER process. In spite of the similar chemical and electronic properties of oxygen, sulfur and selenium anions in $NiCo_2A_4$, their electrochemical properties are still strongly affected by the different spin-orbit coupling effects between cations and anions [35–38]. Of the relative positions within the group VI elements, the Se possesses the largest atomic radius (R_{Se} : 117 pm; R_S : 104 pm; R_O : 66 pm) and the lowest electronegativity (Se: 2.48; S: 2.58; O: 3.44). This characteristic makes it much easier to transfer the electrons from the electrocatalyst substrate to the adsorbed H^+ . From the perspective of surface engineering, a pristine $NiCo_2A_4$ surface is not beneficial for an inhomogeneous charge distribution to weaken the shackles of H^+ ions in $H_{13}O_6^+$. In order to overcome these limitations and activate $NiCo_2A_4$ electrocatalysts, introducing atomic-scale modifications (such as the engineering of vacancies [39,40], heteroatom doping [41,42], and structural strain [43]) represents promising strategy. Among them, anionic vacancy engineering can introduce abundant point defects in $NiCo_2A_4$ crystals, leading to a rise in local charge density. These anionic vacancies can not only restrain the hydration effect for fast H^+ adsorption, but also lower the energy barriers during the following hydrogen reduction processes.

In this work, a series of anionic vacancy-rich $NiCo_2A_4$ ($A = O, S, Se$) nanowires on nitrogen-doped carbon nanofibers ($V_A-NiCo_2A_4$ -NWs/NCNFs, $A = O, S, Se$) have been successfully prepared by combining a hydrothermal approach and controlled annealing treatment. The electrochemical HER test results and density functional theory (DFT) calculations consistently confirm that $V_A-NiCo_2A_4$ -NWs/NCNFs electrocatalysts display higher electrocatalytic activity than the corresponding vacancy-free $NiCo_2A_4$ -NWs/NCNFs systems. The presence of anionic vacancy in $V_A-NiCo_2A_4$ is beneficial for H^+ capture from hydronium ions, and thus

will weaken the shackles of hydronium ions to accelerate the HER. More importantly, the obtained $V_{Se}-NiCo_2Se_4$ -NWs/NCNFs electrocatalyst shows an optimized overpotential of 168 mV at 10 mA cm^{-2} in acid media and a low Tafel slope of 49.8 mV dec^{-1} , which is much better than those of $V_S-NiCo_2S_4$ -NWs/NCNFs and $V_O-NiCo_2O_4$ -NWs/NCNFs electrocatalysts. These results demonstrate that larger anionic vacancy size favours higher HER performance. Therefore, this work demonstrates the deeper correlation between anionic vacancy and intrinsic HER catalytic activity in multi-transition metal based electrocatalysts and provides novel insights into the design of electrocatalysts with outstanding durability and high efficiency.

2. Experimental section

2.1. Preparation of NCNF

The PAN nanofibers were prepared through a facile single-nozzle electrospinning technique using a commercial electrospinning system (UCALERY Beijing Co., Ltd, China). Typically, 0.9 g of PAN and 0.1 g of urea were dissolved in 9 g of *N, N*-dimethylformamide under vigorous stirring at room temperature to form a homogeneous electrospinning precursor solution. Then the precursor electrospinning solution was loaded into a 20 mL plastic syringe equipped with a stainless needle. Electrospinning process was carried out at a voltage of 15 kV at a feeding rate of 0.15 $mm\ min^{-1}$ through a stainless needle. The distance between the aluminum drum collector and stainless needle was 30 cm. The pre-oxidized process of the PAN nanofiber membrane was conducted at 250 °C in air atmosphere for 1 h with a heating rate of 1 °C min^{-1} . The carbonization of electrospinning nanofibers was operated in a tube furnace under nitrogen atmosphere at 800 °C for 2 h with a heating rate of 5 °C min^{-1} . After that, nitrogen-doped carbon nanofibers were obtained, and denoted as NCNF.

2.2. Preparation of Ni–Co-precursor nanowires on nitrogen-doped carbon nanofibers

Typically, 0.5 mmol of $Ni(NO_3)_2 \cdot 6H_2O$, 1 mmol of $Co(NO_3)_2 \cdot 6H_2O$, and 1.5 mmol of urea were added into 40 mL of deionized (DI) water, which was stirred for 30 min to form a homogeneous solution. Then, a piece of NCNF membrane (2 cm × 4 cm) was immersed into the above solution, and transferred into 80 mL Teflon-lined stainless-steel autoclave. The tightly locked autoclave was maintained at 120 °C for 8 h. After cooling to room temperature naturally, the membrane of Ni–Co-precursor nanowires (Ni–Co-pre-NWs) on nitrogen-doped carbon nanofibers was removed from the solution, washed with DI water and alcohol for several times to remove any unreacted residues, dried at 80 °C overnight, and denoted as Ni–Co-pre-NWs/NCNFs. Except for NCNF template, the pure Ni–Co-pre-NWs powder was obtained *via* the same steps for comparison.

2.3. Preparation of oxygen vacancy-rich $NiCo_2O_4$ nanowires on nitrogen-doped carbon nanofibers

The above Ni–Co-precursor nanowires on nitrogen-doped carbon nanofibers were heated in nitrogen atmosphere at 300 °C, resulting in the generation of oxygen vacancy-rich $NiCo_2O_4$ nanowires on nitrogen-doped carbon nanofibers ($V_O-NiCo_2O_4$ -NWs/NCNFs). For comparison, the pristine $NiCo_2O_4$ nanowires on NCNFs ($NiCo_2O_4$ -NWs/NCNFs) were obtained by annealing Ni–Co-pre-NWs/NCNFs in air atmosphere at 300 °C. In addition, the oxygen vacancy-rich $NiCo_2O_4$ nanowires powder was prepared by annealing pure Ni–Co-pre-NWs powder in nitrogen atmosphere at

300 °C ($V_{O-NiCo_2O_4-NWs}$). Similarly, the $NiCo_2O_4$ nanowires powder was also prepared by annealing pure $Ni-Co$ -pre-NWs powder in air atmosphere at 300 °C ($NiCo_2O_4-NWs$).

2.4. Preparation of sulfur vacancy-rich $NiCo_2S_4$ nanowires on nitrogen-doped carbon nanofibers

Firstly, sodium sulfide ($Na_2S \cdot xH_2O$) was used to prepare a 0.2 M solution in DI water. Then, a piece of $NiCo_2O_4-NWs/NCNFs$ membrane (2 cm × 4 cm) was immersed into 40 mL of the above solution, transferred into 80 mL Teflon-lined stainless-steel autoclave, and reacted at 180 °C for 6 h by using hydrothermal method. After cooling to room temperature, the sample was washed with ethanol and DI water for several times, followed by drying at 80 °C overnight, which was named as $NiCo_2S_4$ nanowires on nitrogen-doped carbon nanofibers ($NiCo_2S_4-NWs/NCNFs$). After high-temperature annealing treatment of $NiCo_2S_4-NWs/NCNFs$ at 450 °C for 6 h, the sulfur vacancy-rich $NiCo_2S_4$ nanowires on nitrogen-doped carbon nanofibers ($V_S-NiCo_2S_4-NWs/NCNFs$) were successfully synthesized. Furthermore, the sulfur vacancy-rich $NiCo_2S_4$ nanowires powder ($V_S-NiCo_2S_4-NWs$) was prepared from $NiCo_2O_4-NWs$ via the same steps as $V_S-NiCo_2S_4-NWs/NCNFs$, except for adding NCNF template.

2.5. Preparation of selenium vacancy-rich $NiCo_2Se_4$ nanowires on nitrogen-doped carbon nanofibers

Typically, 0.25 mmol of Na_2SeO_x was dissolved into 35 mL of DI water. Then, a piece of $NiCo_2O_4-NWs/NCNFs$ membrane (2 cm × 4 cm) was immersed into the above solution. After dropping 5 mL of N_2H_4 , the mixture was refluxed at 180 °C for 2 h. After cooling to room temperature, the sample was washed with DI water and ethanol for several times, followed by drying at 80 °C for overnight. Subsequently, the $NiCo_2Se_4$ nanowires on nitrogen-doped carbon nanofibers ($NiCo_2Se_4-NWs/NCNFs$) membrane was annealed in Ar/H_2 atmosphere ($Ar:H_2 = 95:5$, in volume) at 600 °C for 6 h with a heating rate of 5 min^{-1} , to obtain selenium vacancy-rich $NiCo_2Se_4$ nanowires on nitrogen-doped carbon nanofibers ($V_{Se}-NiCo_2Se_4-NWs/NCNFs$). Similarly, the selenium vacancy-rich $NiCo_2Se_4$ nanowires powder ($V_{Se}-NiCo_2Se_4-NWs$) was prepared from $NiCo_2O_4-NWs$ via the same steps as $V_{Se}-NiCo_2Se_4-NWs/NCNFs$, except for adding NCNF template.

2.6. Electrochemical measurements

All electrochemical measurements were conducted on an electrochemical working station (CHI600D, Chenhua Instruments Co. Ltd., Shanghai) in a typical three-electrode configuration at room temperature with 0.5 M H_2SO_4 electrolyte, where graphite rod, and $Ag/AgCl$ reference electrode (3 M KCl) were used as counter and reference electrode, respectively. The linear sweep voltammetry (LSV) was carried out at 5 mV s^{-1} . The stability test was recorded after 1000 CV cycle scanning at 50 mV s^{-1} . The double layer capacitance (C_{dl}) was used to evaluate the active surface areas for composites, where the measured voltages are in a relatively narrow window without faradaic reaction processes. Electrochemical impedance spectroscopy (EIS) measurements was performed using a CHI 660D electrochemistry workstation by applying AC amplitude, with a frequency range from 100 kHz to 0.1 Hz with an amplitude of 5 mV. All polarization curves were corrected with IR drop. Moreover, all potentials in this work were calibrated to corresponding potentials versus the RHE using the equation: $E_{(RHE)} = E_{Ag/AgCl} + 0.212 + 0.0591 \cdot pH$. The typical HER process in acidic solution can be divided into the following two radical steps (Eqs. (1) and (2)):



The values of turnover frequency (TOF) were calculated by assuming that every atom (Ni, Co, O, S, Se) is involved in the catalysis (lower TOF limits were calculated) (Eq. (3)):

$$TOF = \frac{j \times A}{4 \times F \times n} \quad (3)$$

where j (mA cm^{-2}) is the measured current density at $\eta = 200, 250, 300 \text{ mV}$, A is the geometry surface area of electrode, F is Faraday's constant (96485 C mol^{-1}), and n is the moles of coated metal atom on the electrode calculated. The electrochemically active surface areas (ECSA) were estimated by cyclic voltammetry and calibrated. In a narrow potential window, the electrode displays electrical double-layer capacitor mechanism without Faradaic processes, which was used to indicate the active surface areas for comparison. Subsequently, the double layer capacitance (C_{dl}) can be estimated by the half slope of the linearly fitted curve of the capacitive current ($j = j_{anodic} - j_{cathodic}$) plotted against the scan rate.

2.7. Characterization

The morphology of the sample was observed by field-emission scanning electron microscopy (FESEM, Ultra 55) and transmission electron microscopy (TEM, Talos F200S). X-ray diffraction (XRD) patterns were measured using an X'Pert Pro X-ray diffractometer equipped with $Cu K\alpha$ radiation ($\lambda = 0.1542 \text{ nm}$) at a current of 40 mA and voltage of 40 kV. The Raman spectra were collected using a LabRAM-HR Confocal Laser Micro Raman Spectrometer with a 532 nm laser diode as the excitation source. Brunauer-Emmett-Teller (BET) nitrogen adsorption/desorption isotherms were tested by using a Quantachrome Autosorb-iQ/MP®XR system. X-ray photoelectron spectroscopy (XPS) was measured by Thermo Scientific ESCALAB 250Xi equipped with $Al K\alpha$ X-ray source at an energy of 1486.6 eV. The curve fitting of all XPS spectra was accomplished using XPS Peak 4.1 software. All XPS spectra were calibrated according to the C 1s line at 284.8 eV, while curve fitting and background subtraction were accomplished using the RBD AugerScan 3.21 software provided by RBD Enterprises. The liquid phase samples were tested on a Varian 600 MHz spectrometer at ambient temperature, and the chemical shifts were calibrated by CD_3SO .

2.8. Computational methods

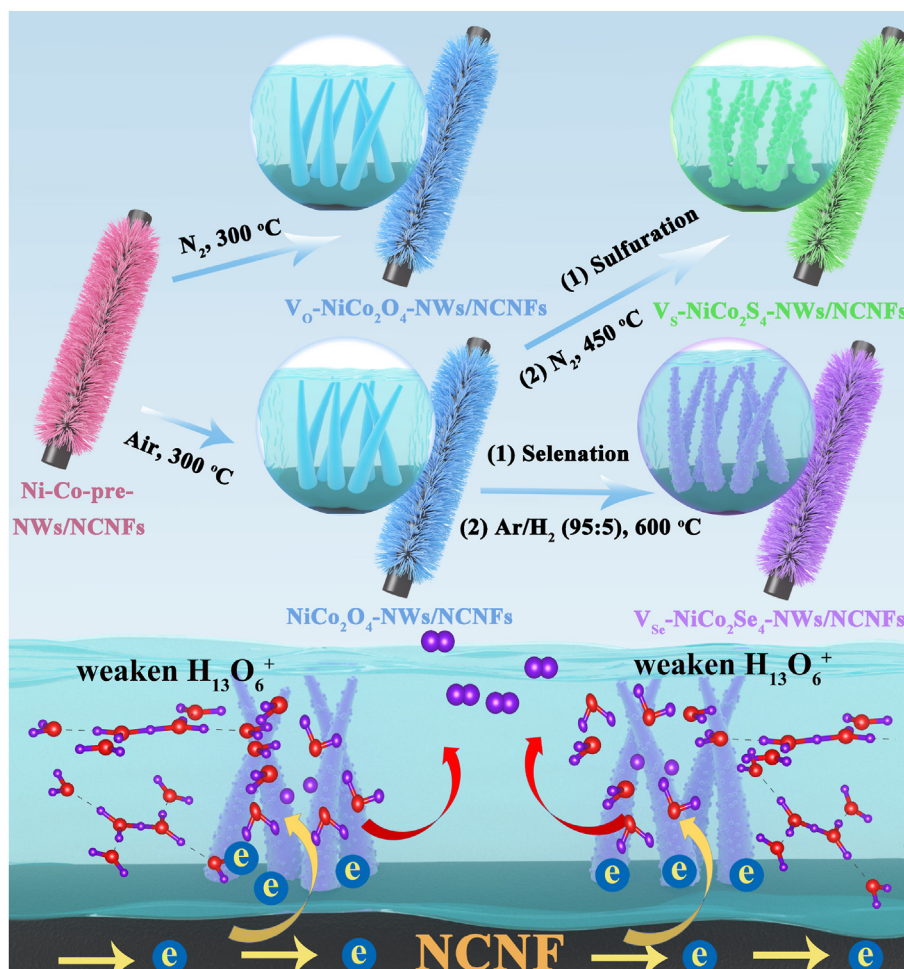
First-principle calculations were performed by density functional theory (DFT), where Vienna Ab-initio Simulation Package (VASP) package is used [44]. The generalized gradient approximation (GGA) with the Perdew–Burke–Ernzerhof (PBE) functional was used to describe the electronic exchange and correlation effects [45]. Spin-polarization was included for their magnetic properties. The calculated lattice constants are $a = b = c = 5.52 \text{ \AA}$ after full relaxation. The K points meshing for Brillouin zone was set up as a $5 \times 11 \times 1$ grid centered at the gamma point regarding Monkhorst Pack Scheme for geometric optimization of the slab surfaces. The simulation was run with a cutoff energy of 450 eV throughout the computations. Spin-polarized density functional theory (DFT) calculations were carried out with the Vienna Ab-initio Simulation Package (VASP) [46], within the projector-augmented wave (PAW) method [47]. The exchange-correlation interaction functional is described by generalized gradient approximation (GGA), in Perdew, Burke, and Ernzerhof (PBE)

functional. The strongly correlated interaction of Co 3d electrons is considered with GGA + U ($U = 4.0$ eV) method [48]. The cutoff energy of 500 eV was adopted for the plane-wave basis set. The structures were relaxed by conjugate gradient algorithm implemented in the VASP code until the forces on the atoms were less than 0.01 eV/Å. The criterion for the total energy is set as 1×10^{-5} eV.

3. Results and discussion

The synthetic process of anionic vacancy-rich NiCo_2A_4 ($A = \text{O}, \text{S}, \text{Se}$) nanowires on nitrogen-doped carbon nanofibers ($\text{V}_A\text{-NiCo}_2\text{A}_4\text{-NWs/NCNFs}$, $A = \text{O}, \text{S}, \text{Se}$) is illustrated in Scheme 1. Briefly, Ni-Co-precursor nanowires are uniformly coated on the nitrogen-doped carbon nanofibers (denoted as Ni-Co-pre-NWs/NCNFs) after a one-step hydrothermal process, the result of which has been characterized using field-emission scanning electron microscopy (FESEM) and X-ray diffraction (XRD), in Figs. S3 and S4, respectively. Under the assistance of an inert N_2 atmosphere, the oxygen atoms in the crystal NiCo_2O_4 nanowires are more likely to escape from the surface with abundant oxygen vacancies left, resulting in the generation of oxygen vacancy-rich NiCo_2O_4 nanowires on nitrogen-doped carbon nanofibers ($\text{V}_\text{O}\text{-NiCo}_2\text{O}_4\text{-NWs/NCNFs}$) [49]. As the SEM image of $\text{V}_\text{O}\text{-NiCo}_2\text{O}_4\text{-NWs/NCNFs}$ (Fig. 1a) shown, its well distributed $\text{V}_\text{O}\text{-NiCo}_2\text{O}_4$ nanowires on the surface of NCNFs maintain the same as that in the $\text{NiCo}_2\text{O}_4\text{-NWs/NCNFs}$ (Figs. S5a and b),

which proves the oxygen vacancy fabrication process would not affect the corresponding morphology. In addition, another two electrocatalysts of sulfur vacancy-rich NiCo_2S_4 nanowires on nitrogen-doped carbon nanofibers ($\text{V}_\text{S}\text{-NiCo}_2\text{S}_4\text{-NWs/NCNFs}$) and selenium vacancy-rich NiCo_2Se_4 nanowires on nitrogen-doped carbon nanofibers ($\text{V}_\text{Se}\text{-NiCo}_2\text{Se}_4\text{-NWs/NCNFs}$) were synthesized through anionic substitution and thermal treatment of $\text{NiCo}_2\text{O}_4\text{-NWs/NCNFs}$, in which sulfur and selenium vacancies can be created owing to the intrinsically higher volatility of the chalcogen atoms in an inert atmosphere [50]. Similarly, the nanowire arrays of $\text{V}_\text{S}\text{-NiCo}_2\text{S}_4\text{-NWs/NCNFs}$ (Figs. S6a and b) and $\text{V}_\text{Se}\text{-NiCo}_2\text{Se}_4\text{-NWs/NCNFs}$ (Fig. 1b) are maintained after the selenation/sulfuration and annealing treatment. Due to the existence of the NCNFs template, the $\text{V}_A\text{-NiCo}_2\text{A}_4$ ($A = \text{O}, \text{S}, \text{Se}$) nanowires are more likely to anchor along the nanofiber direction instead of the generation of $\text{V}_A\text{-NiCo}_2\text{A}_4$ ($A = \text{O}, \text{S}, \text{Se}$) aggregations (Figs. S5c and d, S6d, S7c and d), which is beneficial to increasing the specific surface area, as well as the number of active sites for the following electrochemical reactions. By taking $\text{V}_\text{Se}\text{-NiCo}_2\text{Se}_4\text{-NWs/NCNFs}$ and selenium vacancy-rich NiCo_2Se_4 nanowires ($\text{V}_\text{Se}\text{-NiCo}_2\text{Se}_4\text{-NWs}$) powder as a couple of contrasting examples, their nitrogen adsorption-desorption isotherms and the pore size distributions are provided in Fig. S8. The $\text{V}_\text{Se}\text{-NiCo}_2\text{Se}_4\text{-NWs/NCNFs}$ shows a higher specific surface area (SSA) ($120.5 \text{ m}^2 \text{ g}^{-1}$) than that ($98.5 \text{ m}^2 \text{ g}^{-1}$) of $\text{V}_\text{Se}\text{-NiCo}_2\text{Se}_4\text{-NWs}$ powder. Revealed by the pore size distribution curves (Fig. S8b), both of the $\text{V}_\text{Se}\text{-NiCo}_2\text{Se}_4\text{-NWs/}$



Scheme 1. Schematic illustration of the synthesis process of $\text{V}_A\text{-NiCo}_2\text{A}_4\text{-NWs/NCNFs}$ ($A = \text{O}, \text{S}, \text{Se}$) electrocatalysts, as well as the HER pathways on the corresponding surface.

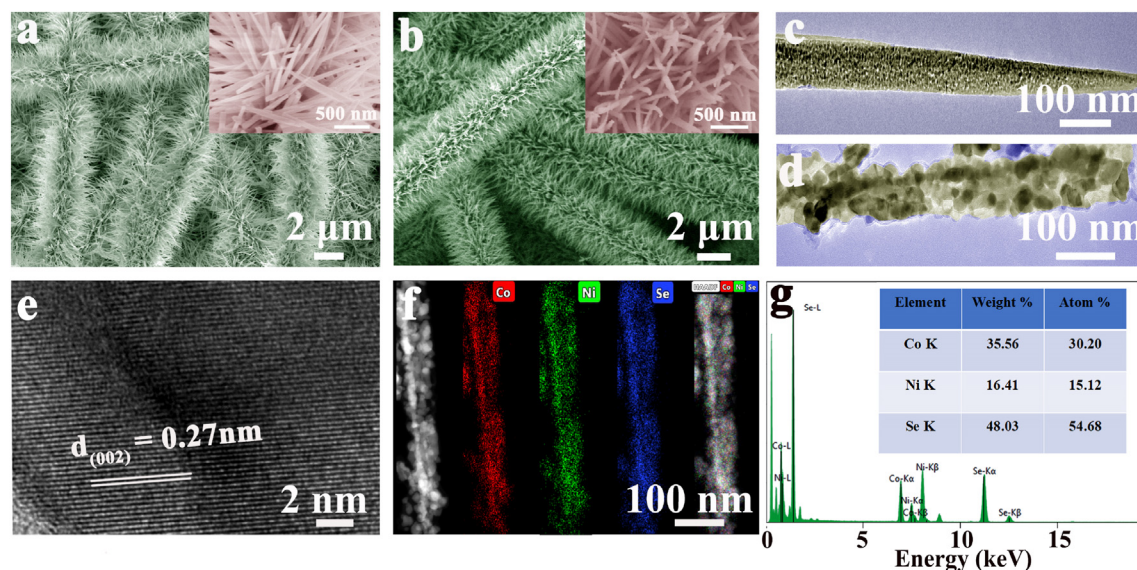


Fig. 1. SEM images of (a) V_0 -NiCo₂O₄-NWs/NCNFs (Inset: under a high magnification), (b) V_{Se} -NiCo₂Se₄-NWs/NCNFs (Inset: under a high magnification), TEM images of (c) V_0 -NiCo₂O₄-NWs/NCNFs, (d) V_{Se} -NiCo₂Se₄-NWs/NCNFs. (e) HRTEM image of V_{Se} -NiCo₂Se₄-NWs/NCNFs. (f) HAADF-STEM and the element mapping images of Co, Ni and Se elements in V_{Se} -NiCo₂Se₄-NWs/NCNFs. (g) EDX spectrum of V_{Se} -NiCo₂Se₄-NWs/NCNFs.

NCNFs and V_{Se} -NiCo₂Se₄-NWs present well-developed mesopores with pore diameters of 3–5 nm. Transmission electron microscopy (TEM) images of V_0 -NiCo₂O₄-NWs/NCNFs and V_{Se} -NiCo₂Se₄-NWs/NCNFs are provided in Fig. 1c and d, which show that the diameters of the corresponding nanowires are around 80 and 100 nm, respectively. The high-resolution transmission electron microscopy (HRTEM) image of the V_{Se} -NiCo₂Se₄-NWs/NCNFs (Fig. 1e) clearly shows a lattice spacing of 0.27 nm, corresponding to the (002) facet of NiCo₂Se₄. This result demonstrates that the potential introduction of selenium vacancies has little impacts on the main crystal structure of NiCo₂Se₄. Energy-dispersive X-ray (EDX) spectroscopy of high-angle annular dark-field scanning transmission electron microscopy (HAADF-STEM) was employed (Fig. 1f and g), which further confirms the homogeneous distribution of Co, Ni and Se elements in V_{Se} -NiCo₂Se₄-NWs/NCNFs. Moreover, the phase purity and crystal structure of V_A -NiCo₂A₄-NWs/NCNFs (A = O, S, Se) electrocatalysts were tested by XRD. A broad diffraction hump from 20° to 30° was observed in the XRD pattern, which is attributed to the amorphous carbon phase (JCPDS card no. 01-0646) in NCNFs. The XRD patterns of the as-prepared V_A -NiCo₂A₄ (A = O, S, Se) NWs/NCNFs samples match well with those of the standard PDF card of NiCo₂Se₄ (Fig. S9), NiCo₂O₄ (Fig. S10), and NiCo₂S₄ (Fig. S11). It should be noted that the NiCo₂A₄-NWs/NCNFs samples exhibit similar XRD patterns as the V_A -NiCo₂A₄-NWs/NCNF samples, which indicates their crystalline structures were almost unchanged after the introduction of anionic vacancies.

X-ray photoelectron spectroscopy (XPS) spectra were recorded to probe the chemical states and generation of anionic vacancies in V_A -NiCo₂A₄-NWs/NCNFs. As illustrated in Fig. 2a, Ni 2p_{3/2} (855.8 eV) and Ni 2p_{1/2} (873.4 eV) in V_{Se} -NiCo₂Se₄-NWs/NCNFs are observed with a negative shift of 0.2 eV when compared with those of NiCo₂Se₄-NWs/NCNFs (Ni 2p_{3/2}: 856.0 eV; Ni 2p_{1/2}: 873.6 eV). Similarly, the peaks of the binding energies for Co 2p_{3/2} (780.8 eV) and Co 2p_{1/2} (796.8 eV) in V_{Se} -NiCo₂Se₄-NWs/NCNFs are also negatively shifted after the introduction of Se vacancies (Fig. 2b) [51–53]. Furthermore, the negative shifts of binding energies with values of ~0.1 eV for both Se 3d_{5/2} and Se 3d_{3/2} peaks in V_{Se} -NiCo₂Se₄-NWs/NCNFs (Fig. 2c) provide the best evidence for the generation of Se vacancies [54,55]. In addition, the high-

resolution N 1s spectrum of V_{Se} -NiCo₂Se₄-NWs/NCNFs (Fig. 2d) can be deconvoluted into three nitrogen-containing species: pyridinic-N (398.4 eV), pyrrolic-N (399.7 eV) and graphitic-N (400.8 eV). These binding energy values exhibit positive shifts of 0.4, 0.3, and 0.3 eV for pyridinic-N, pyrrolic-N, and graphitic-N, respectively, when compared with those in NCNFs. These negative shifts in the binding energies of Co 2p and Ni 2p, and the positive shift in N 1s, indicate the electrons are easier to transfer from the NCNFs host to outside V_{Se} -NiCo₂Se₄ arrays due to their excellent electronic interactions. The tight interfacial connection between V_{Se} -NiCo₂Se₄ and NCNFs is beneficial to generate a charge-rich boundary for fast electron transport during HER [56,57]. In addition, the successful introduction of oxygen and sulfur vacancies in V_0 -NiCo₂O₄-NWs/NCNFs and V_S -NiCo₂S₄-NWs/NCNFs is also demonstrated in the Supporting Information (Figs. S12 and S13).

To investigate the role of the anionic vacancy in V_A -NiCo₂A₄-NWs/NCNFs for the HER electrocatalysis, a standard three-electrode system was operated in 0.5 M H₂SO₄ aqueous electrolyte. Meanwhile, commercial Pt/C was also evaluated for comparison. The IR-corrected polarization curves and Tafel plots of V_A -NiCo₂A₄-NWs/NCNFs and Pt/C are showed in Fig. 3a and b. Notably, the V_{Se} -NiCo₂Se₄-NWs/NCNFs electrocatalyst displays not only the lowest overpotential of 168 mV at a current density of 10 mA cm⁻² (Fig. 3c), but also the smallest Tafel slope of 49.8 mV dec⁻¹ among three V_A -NiCo₂A₄-NWs/NCNFs samples. Meanwhile, the V_A -NiCo₂A₄-NWs/NCNFs show lower overpotential values and smaller Tafel slopes than the corresponding pristine counterparts (Fig. S14), demonstrating the incorporation of anionic vacancy efficiently boosts the electrocatalytic activity. The high electrocatalytic performance of V_{Se} -NiCo₂Se₄-NWs/NCNFs even approaches that of the commercial Pt/C electrocatalyst, while its low cost and tunable structure have the potential to be optimized for renewable hydrogen energy production. Additionally, electrochemical impedance spectroscopy (EIS) was performed to study the various loss mechanisms for each system. The Nyquist plots in Fig. 3d show that the V_{Se} -NiCo₂Se₄-NWs/NCNFs electrocatalyst has the smallest transport resistances among three V_A -NiCo₂A₄-NWs/NCNFs electrocatalysts, which means its fastest electron-transfer process

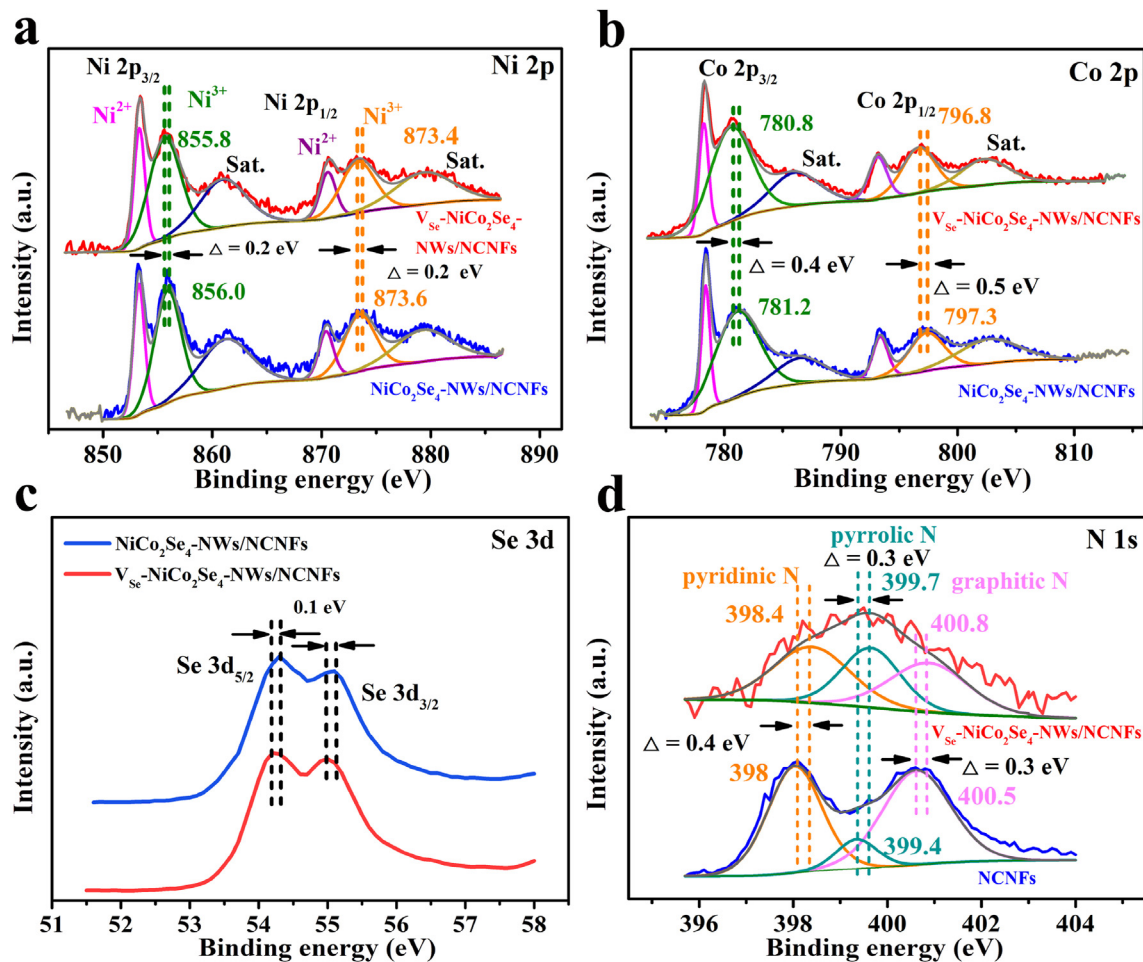


Fig. 2. XPS spectra of (a) Ni 2p, (b) Co 2p, (c) Se 3d of $V_{Se}-NiCo_2Se_4-NWs/NCNFs$ and $NiCo_2Se_4-NWs/NCNFs$. (d) XPS spectra of N 1s of $V_{Se}-NiCo_2Se_4-NWs/NCNFs$ and $NCNFs$.

during HER steps. This could be attributed from the tight interfacial connection between $V_{Se}-NiCo_2Se_4$ nanowires and highly conductive NCNFs support for enhanced interfacial electronic conductivity. Meanwhile, both of the intrinsic and superficial electrical structures in $V_{Se}-NiCo_2Se_4-NWs/NCNFs$ electrocatalyst are well modulated after incorporating anionic vacancies, leading to an increased number of active sites for boosted HER process due to the enhanced electron transfer. The electrochemical double-layer capacitance (EDLC) tested by CV curves (Fig. S15) was used to measure the electrochemical surface areas of different samples (Fig. 3e). The C_{dl} value of $V_{Se}-NiCo_2Se_4-NWs/NCNFs$ (14.9 mF cm^{-2}) is much higher than those of $V_S-NiCo_2Se_4-NWs/NCNFs$ (11.1 mF cm^{-2}) and $V_O-NiCo_2Se_4-NWs/NCNFs$ (3.9 mF cm^{-2}), proving the fact that $V_{Se}-NiCo_2Se_4-NWs/NCNFs$ has the largest active surface area and larger surface coverage of active sites. Turnover frequency (TOF) value is a crucial factor in revealing the catalytic activity of electrocatalysts. Among the three $V_A-NiCo_2A_4-NWs/NCNFs$ electrocatalysts, the as-prepared $V_{Se}-NiCo_2Se_4-NWs/NCNFs$ shows the highest TOF value as 0.453 s^{-1} at an overpotential of 250 mV, which is much larger than those of the corresponding sulfide (0.119 s^{-1}) and oxide samples (0.014 s^{-1}) (Fig. S16). Similarly, $V_A-NiCo_2A_4-NWs/NCNFs$ exhibit higher TOF value than pristine $NiCo_2A_4-NWs/NCNFs$ samples based on Eq. (3) (Fig. S17), which indicates the enhanced atom-utilization efficiency among three $V_A-NiCo_2A_4-NWs/NCNFs$ samples and thus exposes more active sites for HER process. Finally, the long-term durability of $V_{Se}-NiCo_2Se_4-NWs/NCNFs$ was evaluated by performing CV scanning over 1000

cycle (Fig. 3f), which only shows slight degradation and suggests its outstanding durability. A comparison of $V_{Se}-NiCo_2Se_4-NWs/NCNFs$ with other reported HER electrocatalysts in acid media is provided in Table S1, where the $V_{Se}-NiCo_2Se_4-NWs/NCNFs$ shows superior catalytic performance than most transition metal-based for HER catalysis.

To better understand the reason for the enhanced HER catalytic performance, density functional theory (DFT) calculations were applied to study the relationship between anionic vacancy and electrocatalytic activity for HER by constructing the simplified models (Fig. 4a, b and Figs. S19–S22). As revealed by the density of states (DOS) of $NiCo_2O_4$, $NiCo_2S_4$, and $NiCo_2Se_4$ (Fig. 4c and Fig. S22), the $NiCo_2Se_4$ crystal displays the highest intensity near the Fermi level, which demonstrates the superior electrical properties of $NiCo_2Se_4$ (particularly in the electrical conductivity and carrier concentration). It corresponds well with EIS results, where the interfacial electronic conductivity could be enhanced with the substitution of anion. Furthermore, the generated V_{Se} in $V_{Se}-NiCo_2Se_4$ also enhances its DOS intensity near the Fermi level (Fig. 4d), which contributes to its higher charge density and better electrical conductivity than pristine $NiCo_2Se_4$. It is in agreement with the enhanced HER catalytic activity shown in Fig. 3a and Fig. S14. This implies that the highest potential for the adsorption of H^+ ions near the Se vacancy in $NiCo_2Se_4$ and this differential charge distribution can provide more active sites for electrochemical reactions, making the following HER steps much easier.

To further uncover the HER mechanism, the chemical

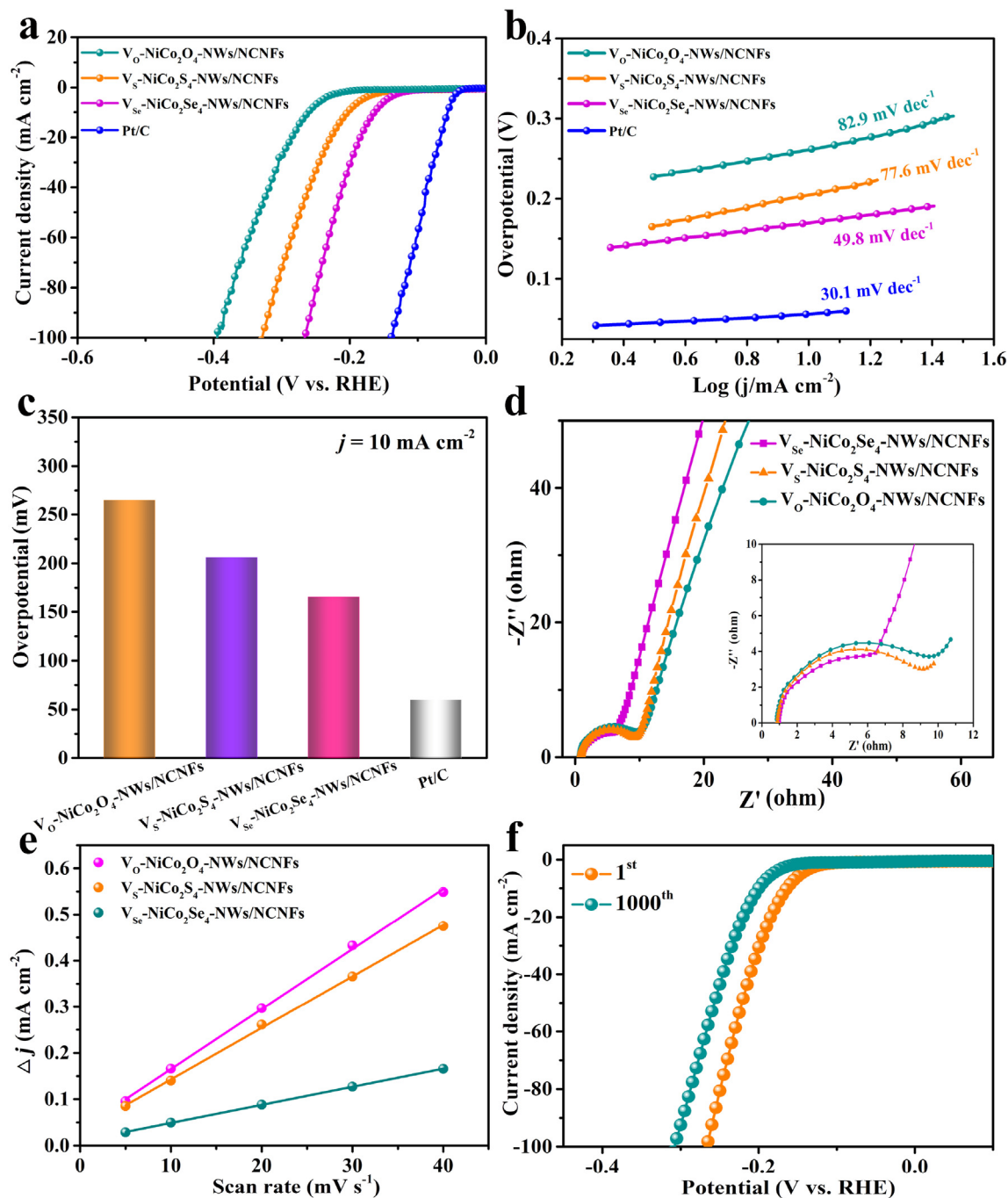


Fig. 3. (a) Polarization curves, (b) Tafel plots, and (c) overpotentials at 10 mA cm^{-2} of $\text{V}_o\text{-NiCo}_2\text{O}_4\text{-NWs/NCNFs}$, $\text{V}_s\text{-NiCo}_2\text{S}_4\text{-NWs/NCNFs}$, $\text{V}_{se}\text{-NiCo}_2\text{Se}_4\text{-NWs/NCNFs}$, and Pt/C in $0.5 \text{ M H}_2\text{SO}_4$ solution. (d) Nyquist plots of $\text{V}_o\text{-NiCo}_2\text{O}_4\text{-NWs/NCNFs}$, $\text{V}_s\text{-NiCo}_2\text{S}_4\text{-NWs/NCNFs}$, $\text{V}_{se}\text{-NiCo}_2\text{Se}_4\text{-NWs/NCNFs}$. (e) Plots showing the extraction of the C_{dl} for the estimation of the ECSA. (f) Stability tests by measuring the polarization profiles for catalyst $\text{V}_{se}\text{-NiCo}_2\text{Se}_4\text{-NWs/NCNF}$ before and after 1000 cycles.

environment of hydronium ions in $0.5 \text{ M H}_2\text{SO}_4$ electrolyte was investigated using ^1H nuclear magnetic resonance ($^1\text{H NMR}$). As shown in Fig. 4f, three $^1\text{H NMR}$ signals at ~ 4.3 , ~ 4.7 , and ~ 6.9 ppm were obtained in $0.5 \text{ M H}_2\text{SO}_4$ electrolyte, in comparison to only one $^1\text{H NMR}$ signal at ~ 4.5 ppm in pure water; these three signals are ascribed to HSO_4^- , water and $\text{H}_{13}\text{O}_6^+$, respectively. A slight positive shift of ~ 0.2 ppm for the water and an obvious negative shift for H^+ ions were observed in $0.5 \text{ M H}_2\text{SO}_4$ electrolyte when compared to those of pure water (4.3 ppm) and concentrated H_2SO_4 (10.8 ppm), respectively. These results imply that H^+ ions in $0.5 \text{ M H}_2\text{SO}_4$ electrolyte are surrounded by coordinated water

molecules with the existence of hydronium ions. Due to the generation of anionic vacancies on the surface of NiCo_2A_4 , the shackles of hydronium ions are significantly weakened with more exposed H^+ ions adsorbed near the vacancy-enriched domains. It can be concluded that the four reaction steps of the HER process on the surface of $\text{V}_{se}\text{-NiCo}_2\text{Se}_4\text{-NWs/NCNFs}$ catalyst can be summarized as shown in Fig. 4g, which includes adsorption of hydronium ions (step i), the capture of H^+ from hydronium ions and the adsorption of H^+ (steps ii and iii), and finally desorption of H_2 (step iv).

Based on the structural analysis and theoretical calculations, the superior electrocatalytic performance of the $\text{V}_{se}\text{-NiCo}_2\text{Se}_4\text{-NWs/}$

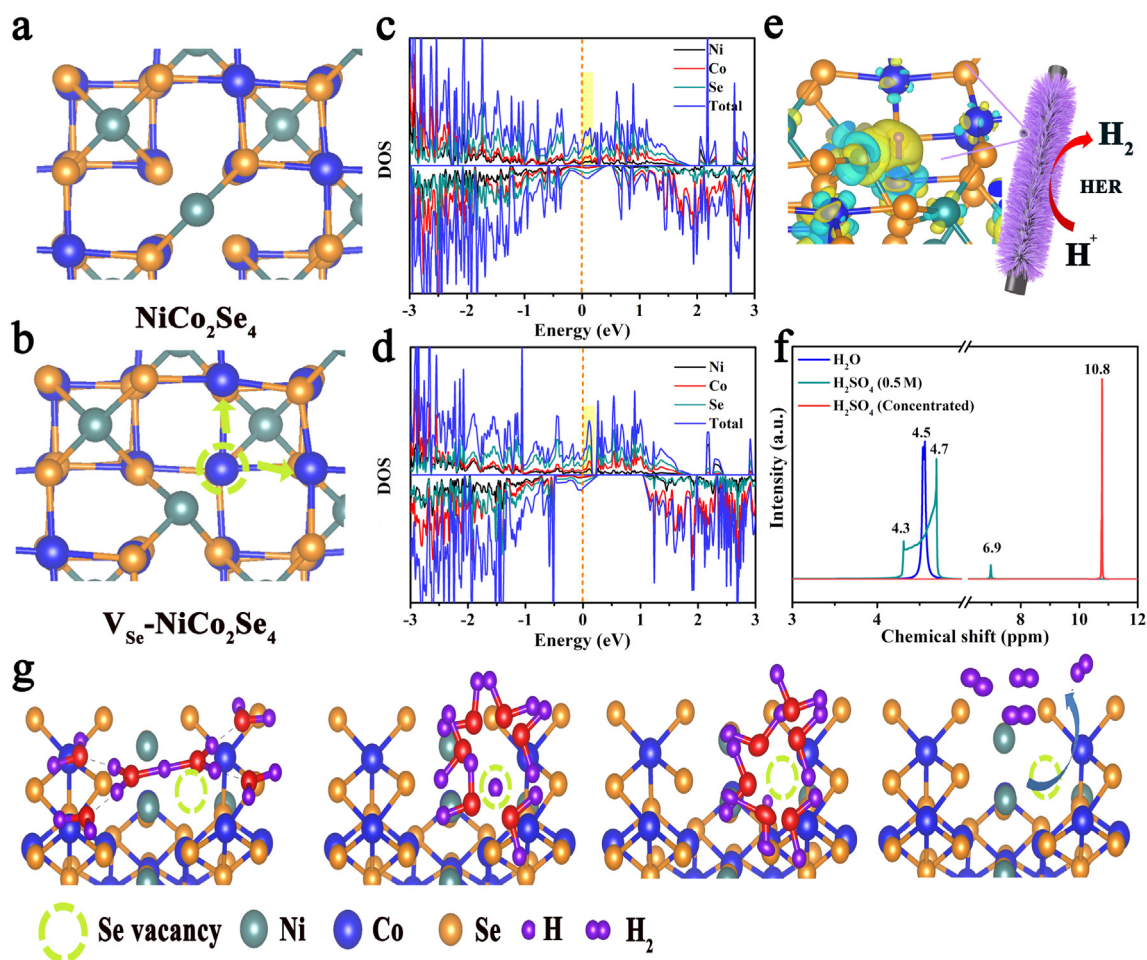


Fig. 4. Simulated models of (a) pristine NiCo_2Se_4 , and (b) NiCo_2Se_4 with selenides vacancies. Calculated DOS for (c) pristine NiCo_2Se_4 , and (d) NiCo_2Se_4 with selenides vacancy. The Fermi level is set at 0 eV. (e) The differential charge density of NiCo_2Se_4 with selenides vacancy. (f) ^1H NMR spectra of water, 0.5 M H_2SO_4 electrolyte and concentrated H_2SO_4 . (g) Reaction steps for HER processes on the surface of $\text{V}_{\text{Se}}\text{-NiCo}_2\text{Se}_4$ NCNFs.

NCNFs could be attributed to the following reasons. Firstly, attributing to the anionic substitution by using homogeneous elements with larger atomic radius ($\text{O} < \text{S} < \text{Se}$), NiCo_2Se_4 possesses a better conductivity compared to both of NiCo_2S_4 and NiCo_2O_4 . Secondly, the group VI anionic vacancy significantly weakens the shackles of H^+ from hydronium ions, which promotes the adsorption of H^+ and thus facilitates the HER process. Finally, the synergistic effect of anionic vacancy and 3D networks of nitrogen-doped carbon nanofibers enhance the conductivity, so promoting the supply of electrons from the inner carbon support to the adsorbed H^+ ions on the surface.

4. Conclusions

In conclusion, a series of anionic vacancy-rich NiCo_2A_4 nanowires on nitrogen-doped carbon nanofibers ($\text{V}_A\text{-NiCo}_2\text{A}_4\text{-NWs/NCNFs}$, $\text{A} = \text{O}, \text{S}, \text{Se}$) have been successfully fabricated by combining a hydrothermal approach and controlled annealing treatment. The electrochemical HER test results and density functional theory calculations consistently confirm that $\text{V}_A\text{-NiCo}_2\text{A}_4\text{-NWs/NCNFs}$ electrocatalysts display higher electrocatalytic activity than the corresponding vacancy-free $\text{NiCo}_2\text{A}_4\text{-NWs/NCNFs}$. This is because the anionic vacancy in $\text{V}_A\text{-NiCo}_2\text{A}_4$ is beneficial to weakening the shackles of hydronium ions, and thus will enhance the H^+ capture for accelerated HER processes. For example, the as-obtained

$\text{V}_{\text{Se}}\text{-NiCo}_2\text{Se}_4\text{-NWs/NCNFs}$ electrocatalyst shows an optimized overpotential of 168 mV at 10 mA cm^{-2} , a low Tafel slope of 49.8 mV dec^{-1} , and excellent long-term durability in acid media. Therefore, this work not only discloses the correlation between anionic vacancy engineering and intrinsic HER catalytic activity for multi-transition metal based HER electrocatalyst, but also provides novel insights to design electrocatalysts with outstanding durability and high efficiency.

Author contributions

Wei Zong: Data curation, Investigation, Writing- Reviewing and Editing. **Ruqian Lian:** Methodology, Software. **Guanjie He:** Formal analysis. **Hele Guo:** Formal analysis. **Yue Ouyang:** Formal analysis. **Jing Wang:** Formal analysis. **Feili Lai:** Conceptualization, Data curation, Writing - Review & Editing. **Yue-E Miao:** Resources. **Dewei Rao:** Methodology, Software, Resources. **Dan Brett:** Writing - Review & Editing. **Tianxi Liu:** Writing - Review & Editing, Supervision, Project administration, Funding acquisition.

Acknowledgements

We are really grateful for the financial support from the National Natural Science Foundation of China (51433001, 21674019, 21604010), the Science and Technology Commission of Shanghai

Municipality (16520722100), the Program of Shanghai Academic Research Leader (17XD1400100), the “Chenguang Program” supported by Shanghai Education Development Foundation and Shanghai Municipal Education Commission (16CG39). The computational center of USTC is acknowledged for computational support.

Appendix A. Supplementary data

Supplementary data to this article can be found online at <https://doi.org/10.1016/j.electacta.2019.135515>.

References

- [1] V.R. Stamenkovic, D. Strmcnik, P.P. Lopes, N.M. Markovic, Energy and fuels from electrochemical interfaces, *Nat. Mater.* 16 (2016) 57–69.
- [2] X.M. Xu, Y.B. Chen, W. Zhou, Z.H. Zhu, C. Su, M.L. Liu, Z.P. Shao, A perovskite electrocatalyst for efficient hydrogen evolution reaction, *Adv. Mater.* 28 (2016) 6442–6448.
- [3] H. Wang, S. Xu, C. Tsai, Y. Li, C. Liu, J. Zhao, Y. Liu, H. Yuan, F. Abild-Pedersen, F.B. Prinz, J.K. Norskov, Y. Cui, Direct and continuous strain control of catalysts with tunable battery electrode materials, *Science* 354 (2016) 1031–1036.
- [4] Y. Jiao, Y. Zheng, K. Davey, S.Z. Qiao, Activity origin and catalyst design principles for electrocatalytic hydrogen evolution on heteroatom-doped graphene, *Nat. Energy* 1 (2016) 16130.
- [5] L. Yu, B.Y. Xia, X. Wang, X.W. Lou, General formation of M–MoS₃ (M = Co, Ni) hollow structures with enhanced electrocatalytic activity for hydrogen evolution, *Adv. Mater.* 28 (2016) 92–97.
- [6] J.F. Xie, H. Zhang, S. Li, R.X. Wang, X. Sun, M. Zhou, J.F. Zhou, X.W. Lou, Y. Xie, Defect-rich MoS₂ ultrathin nanosheets with additional active edge sites for enhanced electrocatalytic hydrogen evolution, *Adv. Mater.* 25 (2013) 5807–5813.
- [7] M.K. Liu, P. Zhang, Z.H. Qu, Y. Yan, C. Lai, T.X. Liu, S.Q. Zhang, Conductive carbon nanofiber interpenetrated graphene architecture for ultra-stable sodium ion battery, *Nat. Commun.* 10 (2019) 1–11.
- [8] Z.C. Zhuang, Y. Li, Z.L. Li, F. Lv, Z.Q. Lang, K.N. Zhao, L. Zhou, L. Moskalova, S.J. Guo, L.Q. Mai, MoB/g-C₃N₄ interface materials as a Schottky catalyst to boost hydrogen evolution, *Angew. Chem. Int. Ed.* 57 (2018) 496–500.
- [9] X.F. Wang, Y.M. Qian, L.N. Wang, H. Yang, H.L. Li, Y. Zhao, T.X. Liu, Sulfurized polyacrylonitrile cathodes with high compatibility in both ether and carbonate electrolytes for ultrastable lithium–sulfur batteries, *Adv. Funct. Mater.* 29 (2019) 1902929.
- [10] M.K. Debe, Electrocatalyst approaches and challenges for automotive fuel cells, *Nature* 486 (2012) 43–51.
- [11] Z. Zhang, G. Liu, X. Cui, B. Chen, Y. Zhu, Y. Gong, F. Saleem, S. Xi, Y. Du, A. Borgna, Z. Lai, Q. Zhang, B. Li, Y. Zong, Y. Han, L. Gu, H. Zhang, Crystal phase and architecture engineering of lotus-thalamus-shaped Pt–Ni anisotropic superstructures for highly efficient electrochemical hydrogen evolution, *Adv. Mater.* 30 (2018) 1801741.
- [12] Y.C. Huang, J.X. Ge, J. Hu, J.W. Zhang, J. Hao, Y.G. Wei, Nitrogen-doped porous molybdenum carbide and phosphide hybrids on a carbon matrix as highly effective electrocatalysts for the hydrogen evolution reaction, *Adv. Energy Mater.* 8 (2018) 1701601.
- [13] H.T. Xu, J. Wan, H.J. Zhang, L. Fang, L. Liu, Z.Y. Huang, J. Li, X. Gu, Y. Wang, A new platinum-like efficient electrocatalyst for hydrogen evolution reaction at all pH: single-crystal metallic interweaved V₈C₇ networks, *Adv. Energy Mater.* 8 (2018) 1800575.
- [14] Y. Yang, S. Niu, D. Han, T. Liu, G. Wang, Y. Li, Progress in developing metal oxide nanomaterials for photoelectrochemical water splitting, *Adv. Energy Mater.* 7 (2017) 1700555.
- [15] T.T. Zheng, W. Sang, Z.H. He, Q.S. Wei, B.W. Chen, H.L. Li, C. Cao, R.J. Huang, X.P. Yan, B.C. Pan, S.M. Zhou, J. Zeng, Conductive tungsten oxide nanosheets for highly efficient hydrogen evolution, *Nano Lett.* 17 (2017) 7968–7973.
- [16] X.B. Zhu, L.L. Mo, Y. Wu, F.L. Lai, X. Han, X.Y. Ling, T.X. Liu, Y.E. Miao, Self-supported MoS₂@NHCF fiber-in-tube composites with tunable voids for efficient hydrogen evolution reaction, *Compos. Commun.* 9 (2018) 86–91.
- [17] W. Zong, F.L. Lai, G.J. He, J.R. Feng, W. Wang, R.Q. Lian, Y.E. Miao, G.C. Wang, I.P. Parkin, T.X. Liu, Sulfur-deficient bismuth sulfide/nitrogen-doped carbon nanofibers as advanced free-standing electrode for asymmetric supercapacitors, *Small* 14 (2018) 1801562.
- [18] Y.P. Huang, Y.E. Miao, J. Fu, S. Mo, C. Wei, T.X. Liu, Perpendicularly oriented few-layer MoSe₂ on SnO₂ nanotubes for efficient hydrogen evolution reaction, *J. Mater. Chem. A* 3 (2015) 16263–16271.
- [19] P. Chen, K. Xu, S. Tao, T. Zhou, Y. Tong, H. Ding, L. Zhang, W. Chu, C. Wu, Y. Xie, Phase-transformation engineering in cobalt diselenide realizing enhanced catalytic activity for hydrogen evolution in an alkaline medium, *Adv. Mater.* 28 (2016) 7527–7532.
- [20] F.L. Lai, D.Y. Yong, X.L. Ning, B.C. Pan, Y.E. Miao, T.X. Liu, Bionanofiber assisted decoration of few-layered MoSe₂ nanosheets on 3D conductive networks for efficient hydrogen evolution, *Small* 13 (2017) 1602866.
- [21] C.A. Reed, The nature of H⁺ in condensed media, *Acc. Chem. Res.* 46 (2013) 2567–2575.
- [22] E.S. Stoyanov, G. Gunbas, N. Hafezi, M. Mascal, I.V. Stoyanova, F.S. Tham, C.A. Reed, The R₃O⁺ ··· H⁺ hydrogen bond: toward a tetracoordinate oxadonimium (2+) ion, *J. Am. Chem. Soc.* 134 (2012) 707–714.
- [23] E.S. Stoyanov, I.V. Stoyanova, C.A. Reed, The structure of the hydrogen ion (H₃O⁺) in water, *J. Am. Chem. Soc.* 132 (2010) 1484–1485.
- [24] J.A. Fournier, W.B. Carpenter, N.H.C. Lewis, A. Tokmakoff, Broadband 2D IR spectroscopy reveals dominant asymmetric H₂O₂⁺ proton hydration structures in acid solutions, *Nat. Chem.* 10 (2018) 932–937.
- [25] H. Fei, J. Dong, Y. Feng, C.S. Allen, C. Wan, B. Voloskiy, M. Li, Z. Zhao, Y. Wang, H. Sun, P. An, W. Chen, Z. Guo, C. Lee, D. Chen, I. Shakir, M. Liu, T. Hu, Y. Li, A.I. Kirkland, X. Duan, Y. Huang, General synthesis and definitive structural identification of MN₄C₄ single-atom catalysts with tunable electrocatalytic activities, *Nat. Catal.* 1 (2018) 63–72.
- [26] J.X. Feng, S.Y. Tong, Y.X. Tong, G.R. Li, Pt-like hydrogen evolution electrocatalysis on PANI/CoP hybrid nanowires by weakening the shackles of hydrogen ions on the surfaces of catalysts, *J. Am. Chem. Soc.* 140 (2018) 5118–5126.
- [27] F.L. Lai, J.R. Feng, X.B. Ye, W. Zong, G.J. He, Y.E. Miao, X.M. Han, X.Y. Ling, I.P. Parkin, B.C. Pan, Y.F. Sun, T.X. Liu, Energy level engineering in transition-metal doped spinel-structured nanosheets for efficient overall water splitting, *J. Mater. Chem. A* 7 (2019) 827–833.
- [28] Y.R. Xue, Z.C. Zuo, Y.J. Li, H.B. Liu, Y.L. Li, Graphdiyne-supported NiCo₂S₄ nanowires: a highly active and stable 3D bifunctional electrode material, *Small* 13 (2017) 1700936.
- [29] Z.W. Fang, L.L. Peng, Y.M. Qian, X. Zhang, Y.J. Xie, J.J. Cha, G.H. Yu, Dual tuning of Ni–Co–A (A = P, Se, O) nanosheets by anion substitution and hole engineering for efficient hydrogen evolution, *J. Am. Chem. Soc.* 140 (2018) 5241–5247.
- [30] X.H. Gao, H.X. Zhang, Q.G. Li, X.G. Yu, Z.L. Hong, X.W. Zhang, C.D. Liang, Z. Lin, Hierarchical NiCo₂O₄ hollow microcuboids as bifunctional electrocatalysts for overall water-splitting, *Angew. Chem. Int. Ed.* 55 (2016) 6290–6294.
- [31] A. Sivanantham, P. Ganesan, S. Shanmugam, Hierarchical NiCo₂S₄ nanowire arrays supported on Ni foam: an efficient and durable bifunctional electrocatalyst for oxygen and hydrogen evolution reactions, *Adv. Funct. Mater.* 26 (2016) 4661–4672.
- [32] Q. Gao, X. Wang, Z. Shi, Z. Ye, W. Wang, N. Zhang, Z. Hong, M. Zhi, Synthesis of porous NiCo₂S₄ aerogel for supercapacitor electrode and oxygen evolution reaction electrocatalyst, *Chem. Eng. J.* 331 (2018) 185–193.
- [33] W. Zhu, M. Ren, N. Hu, W. Zhang, Z. Luo, R. Wang, J. Wang, L. Huang, Y. Suo, J. Wang, Boosting electrocatalytic hydrogen-evolving activity of Co/CoO heterostructured nanosheets via coupling photogenerated carriers with photo-thermy, *ACS Sustain. Chem. Eng.* 6 (2018) 11206–11210.
- [34] Z.W. Fang, L.L. Peng, H.F. Lv, Y. Zhu, C.S. Yan, S.Q. Wang, P. Kalyani, X.J. Wu, G.H. Yu, Metallic transition metal selenide hole nanosheets for efficient oxygen evolution electrocatalysis, *ACS Nano* 11 (2017) 9550–9557.
- [35] P. Ge, C.Y. Zhang, H.S. Hou, B.K. Wu, L. Zhou, S.J. Li, T.J. Wu, J.G. Hu, L.Q. Mai, X.B. Ji, Anions induced evolution of Co₃X₄ (X = O, S, Se) as sodium-ion anodes: the influences of electronic structure, morphology, electrochemical property, *Nano Energy* 48 (2018) 617–629.
- [36] C.P. Yang, S. Xin, Y.X. Yin, H. Ye, J. Zhang, Y.G. Guo, An advanced selenium–carbon cathode for rechargeable lithium–selenium batteries, *Angew. Chem. Int. Ed.* 52 (2013) 8363–8367.
- [37] S. Duhović, M. Dincă, Synthesis and electrical properties of covalent organic frameworks with heavy chalcogens, *Chem. Mater.* 27 (2015) 5487–5490.
- [38] C.P. Yang, Y.X. Yin, Y.G. Guo, Elemental selenium for electrochemical energy storage, *J. Phys. Chem. Lett.* 6 (2015) 256–266.
- [39] B. Liu, Y. Wang, H.Q. Peng, R. Yang, Z. Jiang, X. Zhou, C.S. Lee, H. Zhao, W. Zhang, Iron vacancies induced bifunctionality in ultrathin ferroxhyte nanosheets for overall water splitting, *Adv. Mater.* 30 (2018) 1803144.
- [40] Z. Xiao, Y. Wang, Y.C. Huang, Z. Wei, C.L. Dong, J. Ma, S. Shen, Y. Li, S. Wang, Filling the oxygen vacancies in Co₃O₄ with phosphorus: an ultra-efficient electrocatalyst for overall water splitting, *Energy Environ. Sci.* 10 (2017) 2563–2569.
- [41] S.J. Deng, Y. Zhong, Y.X. Zeng, Y.D. Wang, Z.J. Yao, F. Yang, S.W. Lin, X.L. Wang, X.H. Lu, X.H. Xia, J.P. Tu, Directional construction of vertical nitrogen-doped 1T-2H MoSe₂/graphene shell/core nanoflake arrays for efficient hydrogen evolution reaction, *Adv. Mater.* 29 (2017) 1700748.
- [42] Y. Wu, X. Liu, D. Han, X. Song, L. Shi, Y. Song, S. Niu, Y. Xie, J. Cai, S. Wu, J. Kang, J. Zhou, Z. Chen, X. Zheng, X. Xiao, G. Wang, Electron density modulation of NiCo₂S₄ nanowires by nitrogen incorporation for highly efficient hydrogen evolution catalysis, *Nat. Commun.* 9 (2018) 1425.
- [43] G. Zhang, Y.S. Feng, W.T. Lu, D. He, C.Y. Wang, Y.K. Li, X.Y. Wang, F.F. Cao, Enhanced catalysis of electrochemical overall water splitting in alkaline media by Fe doping in Ni₃S₂ nanosheet arrays, *ACS Catal.* 8 (2018) 5431–5441.
- [44] G. Kresse, J. Furthmüller, Efficiency of ab-initio total energy calculations for metals and semiconductors using a plane-wave basis set, *Comput. Mater. Sci.* 6 (1996) 15–50.
- [45] J.P. Perdew, K. Burke, M. Ernzerhof, Generalized gradient approximation made simple, *Phys. Rev. Lett.* 77 (1996) 3865–3868.
- [46] G. Kresse, J. Hafner, Ab initio molecular dynamics for open-shell transition metals, *Phys. Rev. B* 48 (1993) 13115–13118.
- [47] P.E. Blöchl, Projector augmented-wave method, *Phys. Rev. B* 50 (1994) 17953.
- [48] A.I. Liechtenstein, V.I. Anisimov, J. Zaanen, Density functional theory and

- strong-interactions-orbital ordering in Mott-Hubbard insulators, *Phys. Rev. B* 52 (1995) R5467–R5470.
- [49] J. Bao, X. Zhang, B. Fan, J. Zhang, M. Zhou, W. Yang, X. Hu, H. Wang, B. Pan, Y. Xie, Ultrathin spinel-structured nanosheets rich in oxygen deficiencies for enhanced electrocatalytic water oxidation, *Angew. Chem. Int. Ed.* 54 (2015) 7399–7404.
- [50] M.Q. Yang, J. Wang, H. Wu, G.W. Ho, Noble metal-free nanocatalysts with vacancies for electrochemical water splitting, *Small* 14 (2018) 1703323.
- [51] Y. You, M. Zheng, D. Jiang, F. Li, H. Yuan, Z. Zhai, L. Ma, W. Shen, Boosting supercapacitive performance of ultrathin mesoporous NiCo_2O_4 nanosheet arrays by surface sulfation, *J. Mater. Chem. A* 6 (2018) 8742–8749.
- [52] E. Hu, Y. Feng, J. Nai, D. Zhao, Y. Hu, X.W. Lou, Construction of hierarchical Ni–Co–P hollow nanobricks with oriented nanosheets for efficient overall water splitting, *Energy Environ. Sci.* 11 (2018) 872–880.
- [53] H.L. Guo, Q.C. Feng, K.W. Xu, J.S. Xu, J.X. Zhu, C. Zhang, T.X. Liu, Self-templated conversion of metallogel into heterostructured TMP@carbon quasiaerogels boosting bifunctional electrocatalysis, *Adv. Funct. Mater.* 29 (2019) 1903660.
- [54] Z. Lai, A. Chaturvedi, Y. Wang, T.H. Tran, X. Liu, C. Tan, Z. Luo, B. Chen, Y. Huang, G.H. Nam, Z. Zhang, Y. Chen, Z. Hu, B. Li, S. Xi, Q. Zhang, Y. Zong, L. Gu, C. Kloc, Y. Du, H. Zhang, Preparation of 1T'-Phase $\text{ReS}_{2x}\text{Se}_{2(1-x)}$ ($x=0-1$) nanodots for highly efficient electrocatalytic hydrogen evolution reaction, *J. Am. Chem. Soc.* 140 (2018) 8563–8568.
- [55] C. Tan, Z. Luo, A. Chaturvedi, Y. Cai, Y. Du, Y. Gong, Y. Huang, Z. Lai, X. Zhang, L. Zheng, X. Qi, M.H. Goh, J. Wang, S. Han, X.J. Wu, L. Gu, C. Kloc, H. Zhang, Preparation of high-percentage 1T-phase transition metal dichalcogenide nanodots for electrochemical hydrogen evolution, *Adv. Mater.* 30 (2018) 1705509.
- [56] J.X. Feng, H. Xu, S.H. Ye, G. Ouyang, Y.X. Tong, G.R. Li, Silica–polypyrrole hybrids as high-performance metal-free electrocatalysts for the hydrogen evolution reaction in neutral media, *Angew. Chem. Int. Ed.* 56 (2017) 8120–8124.
- [57] X.B. Li, Y.J. Gao, Y. Wang, F. Zhan, X.Y. Zhang, Q.Y. Kong, N.J. Zhao, Q. Guo, H.L. Wu, Z.J. Li, Y. Tao, J.P. Zhang, B. Chen, C.H. Tung, L.Z. Wu, Self-assembled framework enhances electronic communication of ultrasmall-sized nanoparticles for exceptional solar hydrogen evolution, *J. Am. Chem. Soc.* 139 (2017) 4789–4796.